Najdahmadi, S., Bohnhoff, M., Ben-Zion, Y. (2016): Bimaterial interfaces at the Karadere segment of the North Anatolian Fault, northwestern Turkey. - *Journal of Geophysical Research*, *121*, 2, pp. 931—950.

DOI: http://doi.org/10.1002/2015JB012601

AGU PUBLICATIONS

JGR

Journal of Geophysical Research: Solid Earth

RESEARCH ARTICLE
10.1002/2015JB012601

Key Points:
- We observe fault zone head and reflected phases along the Karadere Fault of the NAFZ
- The fault zone head waves are produced by both deep and shallow bimaterial interfaces
- The deep interface represents the main fault, while the shallow one the damage zone and/or basin

Correspondence to:
B. Najdahmadi,
bita@gfz-potsdam.de

Citation:
Najdahmadi, B., M. Bohnhoff, and Y. Ben-Zion (2016), Bimaterial interfaces at the Karadere segment of the North Anatolian Fault, northwestern Turkey, *J. Geophys. Res. Solid Earth*, *121*, 931–950, doi:10.1002/2015JB012601.

Received 15 OCT 2015
Accepted 21 JAN 2016
Accepted article online 25 JAN 2016
Published online 18 FEB 2016

Bimaterial interfaces at the Karadere segment of the North Anatolian Fault, northwestern Turkey

B. Najdahmadi[1], M. Bohnhoff[1,2], and Y. Ben-Zion[3]

[1]Geomechanics and Rheology, Helmholtz-Centre Potsdam, GFZ German Centre for Geosciences, Potsdam, Germany, [2]Institute of Geological Sciences, Free University Berlin, Berlin, Germany, [3]Department of Earth Sciences, University of Southern California, Los Angeles, California, USA

Abstract We image velocity contrast (bimaterial) interfaces along the Karadere Fault of the North Anatolian Fault Zone, toward the eastern part of the 1999 Izmit M_w 7.4 rupture in NW Turkey, using waveforms recorded by a local seismic network. Applying an automatic procedure for identification and picking of fault zone head waves (FZHW) and direct *P* arrivals, and manually revising the picks through particle motion analysis, we identify two different groups of FZHW as well as fault zone reflected waves (FZRW). The first group of FZHW has a moveout with respect to the direct *P* arrivals with distance traveled along the fault, indicating a deep bimaterial interface down to the base of the seismogenic crust with an average velocity contrast of ~3.4%. The second group of FZHW has a constant time difference from the direct *P* arrivals and is associated with a shallow local interface bounding a low-velocity damage zone or basin structure that extends to a depth of 4–5 km. While the first group of FZHW exists on the slower crustal block, the second group of FZHW and the FZRW are present generally on both sides of the fault. These phases add to the richness and complexity of the early *P* waveforms observed at stations close to a large fault. The relatively low velocity contrast across the Karadere Fault compared to values to the west may have helped stopping the Izmit rupture.

1. Introduction

Large fault zones have bimaterial interfaces that separate different lithologies. These are generated by the long-term offset along the fault, cumulative rock damage products, and other fault-zone-related structures such as basins and mountains. The existence of different rock types within and across fault zones can modify the properties of the local seismic and geodetic fields [e.g., *Ben-Zion and Aki*, 1990; *Le Pichon et al*., 2005; *Özeren and Holt*, 2010]. This is relevant for numerous topics including earthquake locations, focal mechanisms, Moho topography below the fault, delay times of teleseismic waves, interseismic strain fields, and near-fault amplification of ground motion [e.g., *Oppenheimer et al*., 1988; *Ben-Zion and Malin*, 1991; *Schulte-Pelkum and Ben-Zion*, 2012; *Ozakin et al*., 2012; *Wdowinski et al*., 2007; *Kurzon et al*., 2014]. Moreover, bimaterial fault interfaces can significantly affect the mode, dynamic properties, and propagation direction of earthquake ruptures [e.g., *Ben-Zion*, 2001; *Ampuero and Ben-Zion*, 2008; *Lengliné and Got*, 2011; *Calderoni et al*., 2015], along with space-time variations of seismicity along the fault [e.g., *Rubin and Gillard*, 2000; *Zaliapin and Ben-Zion*, 2011] and generation of small-scale local structural properties [e.g., *Dor et al*., 2008; *Wechsler et al*., 2009; *Ben-Zion et al*., 2012].

Basin structures are common along faults and are known to be generated in "pull-apart" places where transtensional deformation separates neighboring crustal blocks by a lateral offset in combination with an extensional stress field [e.g., *Burchfiel and Stewart*, 1966; *Crowell*, 1974; *Sibson*, 1986; *Hubert-Ferrari et al*., 2002; *Bohnhoff et al*., 2006]. In addition to pull-apart basins, local structures with low-velocity rocks can be generated by the cumulative damage process along the fault [e.g., *Lyakhovsky and Ben-Zion*, 2009; *Finzi et al*., 2009]. Broad zones with damaged low-velocity rocks have been documented around numerous large faults based on seismic, gravity, geodetic, and other data. As examples, *Hamiel and Fialko* [2007] inferred on the existence of several kilometer-wide damage zone around the North Anatolian Fault Zone (NAFZ) from interferometric synthetic aperture radar observations associated with the 1999 Izmit earthquake. *Allam and Ben-Zion* [2012] and *Zigone et al*. [2015] imaged with earthquake- and noise-based tomography zones with similar width of reduced seismic velocities around the San Jacinto Fault zone in Southern California.

The best diagnostic signal to detect and study a bimaterial fault interface is provided by fault zone head waves (FZHW) that refract along the interface and are radiated from there to the slow side of the fault [*Ben-Zion*, 1989, 1990]. These waves have been observed and provided information on lithology contrasts at

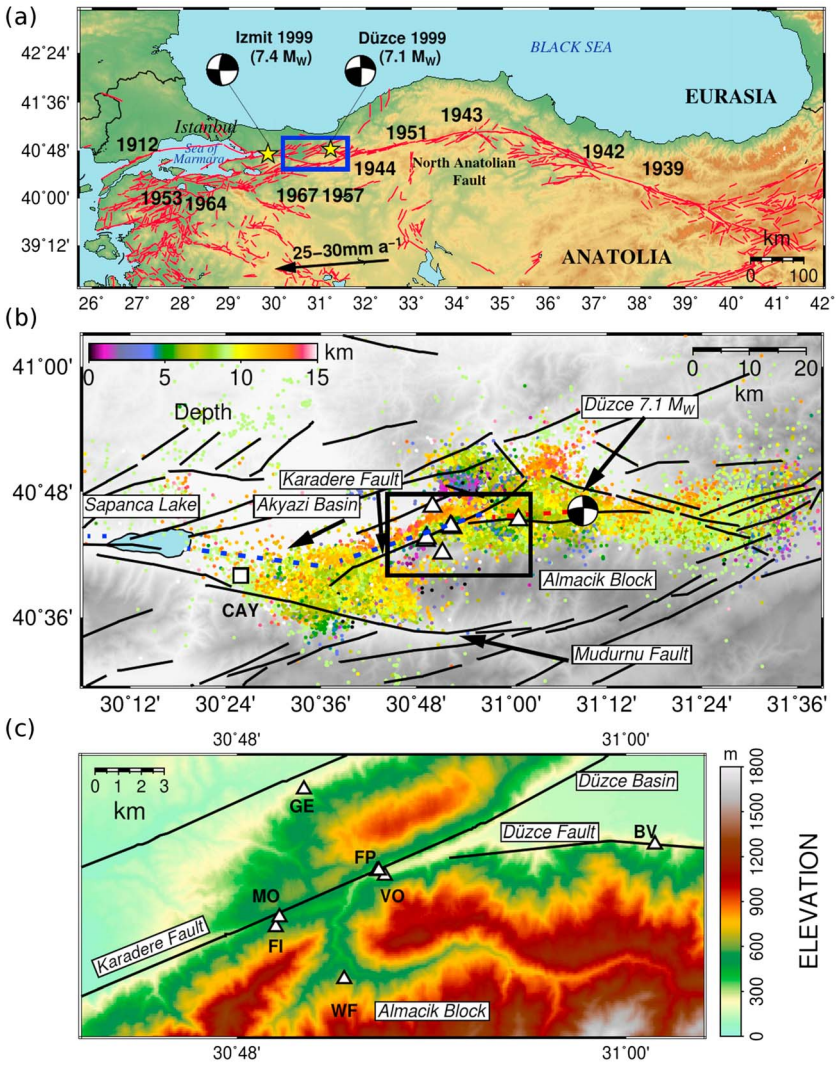

Figure 1. (a) Regional tectonic framework of the northern Anatolian region with the North Anatolian Fault Zone (NAFZ, red lines) as the right-lateral transform plate boundary between Anatolia and Eurasia. Current right-lateral slip along the NAFZ is 20–30 mm/yr increasing from east to west [*McClusky et al.*, 2000]. Black numbers indicate year and location of $M > 7$ earthquakes in the twentieth century. The most recent ones, the 1999 Izmit and Düzce earthquakes are marked by yellow stars with corresponding focal mechanisms (data after *Özalaybey et al.* [2002]). The blue rectangle marks the area of study and is enlarged in Figure 1b. (b) Study area including the eastern part of the Izmit rupture (blue dashed line) and the Düzce rupture (red dashed line) after *Barka et al.* [2002], Sapanca, Akyazi, and Karadere segments, and the Mudurnu Fault (a NAFZ branch that was not activated during the 1999 earthquakes). Additional NAFZ branches and nearby mapped faults are indicated by the black lines (data after http://deprem.gov.tr/). The seismicity represents aftershocks of the Izmit and Düzce events and is color encoded with depth. The focal mechanism shows the location and faulting mechanism of the Düzce earthquake. White triangles are selected seismic stations of the PASSCAL network [*Seeber et al.*, 2000] that were used in this study. The white square is station CAY from the SABONET network [*Milkereit et al.*, 2000], where a velocity contrast across the NAFZ of at least 6% was found [*Bulut et al.*, 2012]. The black rectangle indicates the area of the stations used and is enlarged in Figure 1c. (c) Seismic stations along the Karadere Fault that is bounded by the Düzce Basin and Düzce Fault in the northeast, by the elevated crustal Almacik Block in the southeast.

various places including the subduction zone underneath Japan [e.g., *Fukao et al.*, 1983], several sections of the San Andreas Fault system in California [e.g., *Ben-Zion and Malin*, 1991; *McGuire and Ben-Zion*, 2005; *Zhao and Peng*, 2008; *Zhao et al.*, 2010; *Allam et al.*, 2014], the eastern California shear zone [*Hough et al.*, 1994], the Mudurnu segment of the NAFZ [*Bulut et al.*, 2012], and the Garzê-Yushu Fault in the Tibetan Plateau [*Yang et al.*, 2015].

In a simple structure consisting of two solids in contact, FZHW are the first arrivals at stations on the side with slower seismic velocity that are within a critical distance x_c from the interface given by [*Ben-Zion*, 1989]

$$x_c = r \cdot \tan\left(\cos^{-1}(\alpha_s/\alpha_f)\right), \quad (1)$$

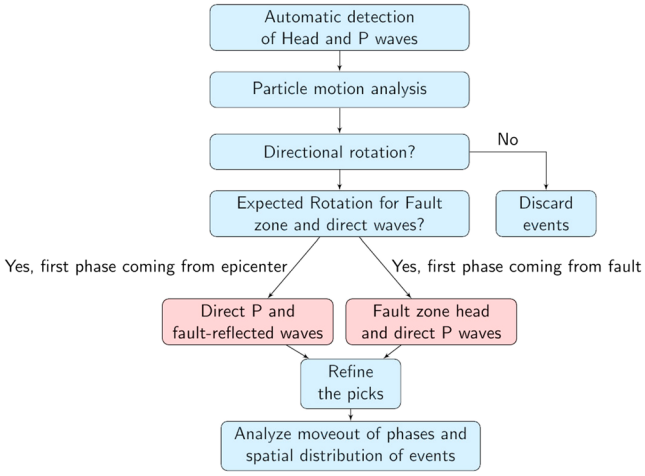

Figure 2. Flow chart showing the data analysis procedure applied in this study. The two important pairs of seismic phases (direct *P* and FZRW, or FZHW and direct *P*) identified and analyzed in this study are indicated in the two pink boxes.

where r is the distance the FZHW travel along the fault and α_f, α_s are the average *P* wave velocities of the faster and slower media, respectively. Several characteristics can be used to identify FZHW: they are emergent, have opposite first-motion polarity than the more impulsive following direct waves and have arrival time moveout (Δt) from the direct wave that increases with distance traveled along the fault (r) as

$$\Delta t \sim r \ \Delta\alpha/\alpha^2, \tag{2}$$

with α and $\Delta\alpha$ denoting the average and differential *P* wave velocities, respectively [*Ben-Zion and Malin*, 1991]. In addition, since FZHW are radiated from the fault they should have particle motion with significant fault-normal component, in contrast to the particle motion of the direct *P* waves that points to the epicenter direction [*Bulut et al.*, 2012; *Allam et al.*, 2014].

In the present paper we use the above properties to identify and analyze FZHW and direct *P* arrivals in near-fault seismic data recorded along the Karadere segment of the NAFZ. In the next section we describe the study area and employed seismic data. In section 3 we perform detailed analysis of the early portions of *P* waveforms recorded close to the Karadere segment. We find abundant evidence for two different groups of FZHW that propagate both along a deep bimaterial interface and along an edge of a shallow low-velocity zone or a basin structure around the fault. In addition to FZHW, we observe secondary *P* waves that appear to be reflected from interfaces in the fault zone structure. We refer to these phases as fault zone reflected waves (FZRW). The results are discussed and summarized in section 4 of the paper.

2. Study Area and Data

The NAFZ is one of the largest plate-bounding transform faults, separating the Anatolian and Eurasian plates and extending for 1200 km between Eastern Anatolia and the Northern Aegean [e.g., *Sengör et al.*, 2005]. Westward movement of Anatolia has developed in the framework of the northward moving Arabian plate and the southward rollback of the Hellenic Subduction Zone where the African lithosphere is subducted below the Aegean [e.g., *Flerit et al.*, 2004; *Bohnhoff et al.*, 2005]. The current right-lateral slip rate along the NAFZ is 20–30 mm/yr [e.g., *Barka*, 1992; *McClusky et al.*, 2000], repeatedly producing major ($M > 7$) strike-slip earthquakes. During the twentieth century, the NAFZ has ruptured over 900 km of its length [*Ambraseys*, 1970; *Barka*, 1999] with a series of large earthquakes migrating overall westward toward the Istanbul-Marmara region in NW Turkey. The most recent major events on the NAFZ occurred in 1999 with the M_w 7.4 Izmit and M_w 7.1 Düzce earthquakes (Figure 1a) [e.g., *Tibi et al.*, 2001], leaving the Marmara section as the only NAFZ portion that has not sustained a major earthquake since 1766 [*Parsons*, 2004; *Bohnhoff et al.*, 2013].

In this paper we study structural properties of the Karadere segment of the NAFZ located toward the eastern part of the 120 km long surface rupture of the Izmit event (Figures 1b and 1c). The Karadere segment is important for understanding the seismomechanical setting of this region, since it is located between the extensional Akyazi and Düzce Basins [*Bulut et al.*, 2007; *Görgün et al.*, 2010]. The Karadere Fault has a local strike of N65°E, while the NAFZ strikes EW on average. The Karadere Fault sustained a right-lateral coseismic slip of about 1.5 m during the Izmit earthquake, which is substantially less than that at the nearby Sapanca segment to the east that had a coseismic displacement of 5–6 m [e.g., *Tibi et al.*, 2001; *Barka et al.*, 2002]. This variation in lateral slip caused EW extensional normal faulting aftershocks at the Akyazi pull-apart basin

Table 1. Parameters Used in the Algorithm of Automatically Picking Fault Zone Head Waves (FZHW) and Direct *P* Waves

Parameter	Value
Maximum velocity contrast	0.1
Minimum distance allowed	0
Corner frequency of high-pass filter (Hz)	0.5
Padding to be added (s) to start of trace if not enough	0
Short-term average (STA) and long-term average (LTA) time windows	0.1, 10
Minimum time separation allowed between FZHW and direct *P*	0.065
P wave velocity on fast side (km/s)	5.5
Sliding window length (sec) for kurtosis/skewness	5
Start/end coordinates of fault	40.7, 30.6–40.77, 31.35

that is located in between (Figure 1b) [*Bohnhoff et al*., 2006]. Further to the east where the Izmit rupture stopped within the transition from the Düzce Fault toward the Düzce Basin, the M_w 7.1 Düzce rupture nucleated after 87 days extending the rupture by ~40 km to the east and rerupturing parts of the Düzce Fault [*Hartleb et al*., 2002; *Hearn et al*., 2002].

Aftershock recordings provided information for detailed studies of the seismotectonic setting after the Izmit and Düzce mainshocks [*Bohnhoff et al*., 2006; *Bulut et al*., 2007; Bohnhoff *et al*., Crustal response to spatiotemporal variations of coseismic slip along the combined 1999 Izmit-Düzce rupture, submitted to *Tectonophysics*, 2015]. The results in part also documented a significant rotation of the local stress tensor [*Ickrath et al*., 2014, 2015] and substantial nondouble components [*Stierle et al*., 2014a, 2014b] below the Akyazi Basin within weeks following the mainshock. The Karadere Segment is located between the Akyazi and Düzce releasing bends and is a steeply (~67°) north dipping strike-slip fault [*Bulut et al*., 2007], reflecting mostly right-lateral strike-slip aftershocks in general correspondence with the regional stress field [*Bohnhoff et al*., 2006; *Görgün et al*., 2010]. At present no information on the crustal velocity structure on the opposite sides of the fault is available. The strongest Izmit aftershock activity occurred at the Akyazi-Karadere-Düzce seismicity cluster located at the northern margin of the elevated crustal Almacik Block separating the NAFZ into northern (Karadere-Düzce) and southern (Mudurnu) branches (Figure 1b). The latter branch had a *M* 7 event in 1967 [*Ambraseys and Zatopek*, 1969] with no major stress buildup since then indicated by the absence of Izmit aftershocks (Figure 1b).

To study the possible existence of bimaterial interfaces in the structure associated with the Karadere Fault, we use waveform data recorded by the local seismic PASSCAL network that was deployed within 1 week after the Izmit earthquake along and around the Karadere-Düzce sections of the NAFZ (Figures 1b and 1c) [*Seeber et al*., 2000; *Ben-Zion et al*., 2003]. The network operated for about 6 months with the goals of monitoring local aftershock activity at low-magnitude detection threshold and studying the subsurface structure of the Karadere-Düzce sections. Most sites had a mixture of three-component L22 sensors and three-component force balance accelerometers. Sites MO (for the full deployment) and GE (for the first 2 months) had three-component broadband (Guralp CMG-40 T) sensors. The choice of location was fortunate since 3 months after the deployment the Düzce earthquake nucleated, propagating back to the network location and farther to the east. The network recorded waveforms at on- and off-fault stations generated by >25,000 earthquakes detected with standard techniques. This data set was used previously to image trapping fault zone structure [*Ben-Zion et al*., 2003], crustal

Table 2. List of the Stations Used in This Analysis With Their Operation Period, Number of the Seismograms that We Analyzed With the Automatic Picker, Number of FZHW Detected After Using the Automatic Picker (Before Any Particle Motion Analysis), Final FZHW Left After the Particle Motion Analysis and the Number of FZRW Found Beside the Final FZHW

Name of Station	Archive Data[a]	Examined Seismograms	Detected FZHW	Final FZHW	Final FZRW
MO	1999/8/26 to 2000/12/31	14,050	420	16	22
FI	1999/9/04 to 2000/2/13	13,100	870	35	36
WF	1999/9/11 to 2000/2/13	17,780	480	31	42
GE	1999/8/27 to 2000/2/12	16,700	250	2	22
FP	1999/10/29 to 2000/2/12	11,300	333	88	41
VO	1999/9/2 to 2000/2/12	19,900	459	11	20
BV	1999/9/14 to 2000/2/12	15,700	547	4	32

[a]Dates in column 2 are formatted as year/month/day.

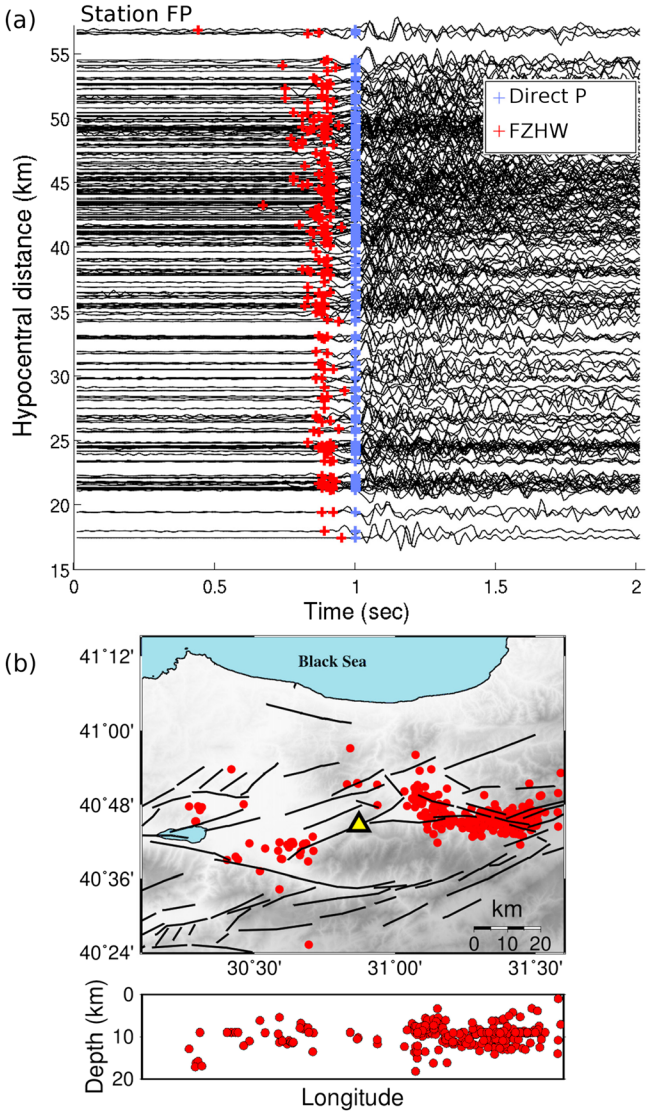

Figure 3. (a) Preliminary results for station FP after running the automatic algorithm to detect direct *P* and FZHW on all vertical seismograms of local events recorded by the station. We only show vertical seismograms on which FZHW (red crosses marking first arrivals) were detected for hypocenters located east of the station. Waveforms are aligned on the direct *P* arrivals (light blue crosses marking second arrivals) and plotted with hypocentral distance. (b) Epicentral map and depth section for the earthquakes used in Figure 3a, as well as hypocenters of events located west of station producing detected FZHW. Station FP is marked with the yellow triangle.

anisotropy [*Peng and Ben-Zion*, 2004, 2005], temporal changes of seismic velocities [*Peng and Ben-Zion*, 2006; *Wu et al.*, 2009], and earthquake source properties [*Yang et al.*, 2009]. However, bimaterial interfaces that are the focus of this work were not targeted for imaging so far. To image bimaterial interfaces we use seven stations from the network that recorded significant amount of data at on- and off-fault locations along the Karadere Fault, including one station (BV) farther east at the Düzce Fault (Figures 1b and 1c).

3. Data Analysis and Results

To analyze the data systematically, we follow the processing steps shown in the flowchart of Figure 2. We begin with comprehensive automatic identification and picking of candidate FZHW and direct *P* arrivals using the algorithm of *Ross and Ben-Zion* [2014] based on various characteristics of both wave types, including first-motion polarities, time difference, sharpness, and amplitude variations. The method was shown to perform well on data recorded near the Parkfield section of the San Andreas Fault, the Hayward Fault, and sections of the San Jacinto Fault zone in California [*Ross and Ben-Zion*, 2014; *Share et al.*, 2015; *Qiu et al.*, 2015]. The algorithm has several parameters including a frequency range for filtering in a preprocessing stage, values of short-term average/long-term average (STA/LTA) time windows, and a range of time differences between FZHW and direct *P* arrivals (corresponding to minimum and maximum expected velocity contrast). The values of the parameters used in this study (Table 1) are the same as those in *Ross and Ben-Zion* [2014].

The locations of the used events were determined by standard analysis with an approximate velocity model [*Seeber et al.*, 2000; *Ben-Zion et al.*, 2003], and they have uncertainties of about 2–3 km or more. The event locations are distributed broadly around the main NAFZ (Figure 1b) reflecting, at least partially, structural complexity in the study area. The location uncertainties prevent us from selecting a subset of events that are highly localized along the fault. Instead, we simply run the automatic picker on all data and analyze candidate detections as summarized in Figure 2 and described below. We examine about 100,000 waveforms at the different stations (Table 2). In most cases the analysis does not provide evidence for fault-related phases, but we detect several hundreds of FZHW that are used for detailed analyses. Figure 3 shows as an example

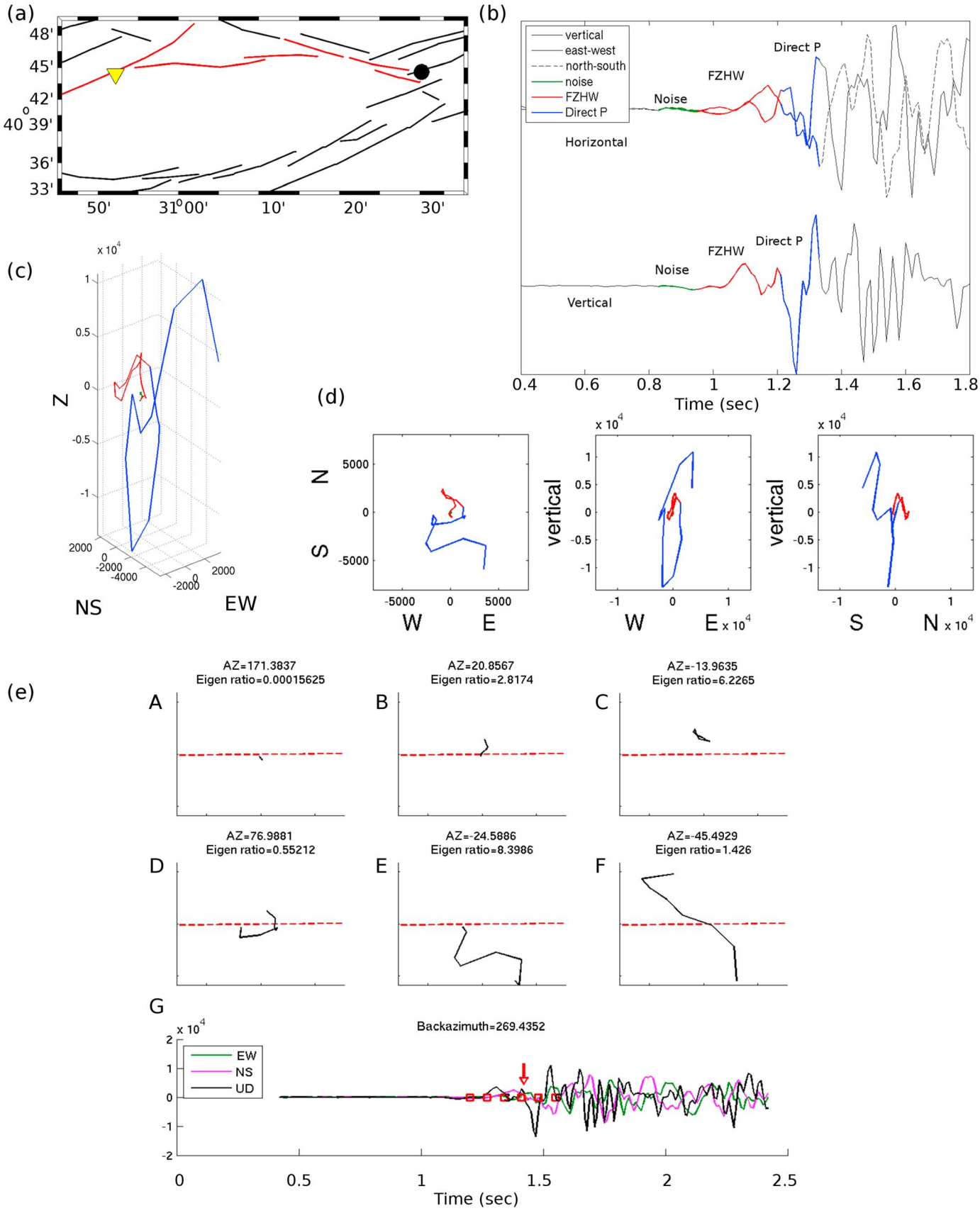
(a)
48'
45'
42'
40°39'
36'
33'
50'
31°00'
10'
20'
30'
(b)
vertical
east-west
north-south
noise
FZHW
Direct P
Horizontal
Noise
FZHW
Direct P
Vertical
Noise
FZHW
Direct P
0.4
0.6
0.8
1
1.2
1.4
1.6
1.8
Time (sec)
(c)
x 10^4
N
NS
EW
(d)
N
S
W
E
vertical
W
E x 10^4
vertical
S
N x 10^4
(e)
AZ=171.3837
Eigen ratio=0.00015625
A
AZ=20.8567
Eigen ratio=2.8174
B
AZ=-13.9635
Eigen ratio=6.2265
C
AZ=76.9881
Eigen ratio=0.55212
D
AZ=-24.5886
Eigen ratio=8.3986
E
AZ=-45.4929
Eigen ratio=1.426
F
G
x 10^4
EW
NS
UD
Backazimuth=269.4352
Time (sec)

detection results for station FP with (a) automatic picks of FZHW and direct *P* waves for hypocenters located east of the station and (b) locations of all events generating detected FZHW by the algorithm of *Ross and Ben-Zion* [2014].

As a first step of our in-depth study we perform particle motion analysis on the FZHW and direct *P* arrivals flagged by the automatic picker, as done and described in detail by *Bulut et al*. [2012] and *Allam et al*. [2014]. If the directions of both waves are similar (e.g., within about 50°) the event is not used for further FZHW analysis. An event is also discarded if the two directions were different, but neither is close to the fault normal direction. However, if the particle motion of one phase points approximately to the fault and the other points approximately to the epicenter of the event, the data are retained for further analysis. If the first phase appears to be radiated from the fault, as found in the previous studies mentioned above, it is labeled FZHW and the following phase is labeled direct *P* wave. In the course of the analysis we found a set of waveforms with reversed order of directions, namely, the first phase points approximately to the epicenter direction and the second pointing to the fault. We also find that in such cases the impulsiveness of the second phase is similar to that of the first. We consider such cases to be associated with first-arriving direct *P* body waves followed by a secondary FZRW reflected from a fault zone interface.

Figure 4 illustrates the particle motion analysis for one example event (Figure 4a) with FZHW and subsequent direct *P* arrival. We examine both the horizontal 2-D (east-west and north-south) and 3-D (vertical component added) particle motion of each waveform before and after the arrival of the FZHW and direct *P* waves as shown in Figures 4b–4d. Following *Allam et al*. [2014], polarizations are also calculated (Figure 4e) in narrow time windows of the displacement seismograms with the algorithm of *Jurkevics* [1988]. FZHW should have larger eigenvalues than the noise and the direct *P* waves should have larger eigenvalues than the FZHW [*Allam et al*., 2014]. The changes in the main azimuth of polarization between the windows corresponding to the FZHW and direct *P* phase should be $>50°$ to satisfy the criterion for retaining the waveform for additional analysis. Figure 5 illustrates similar particle motion analysis leading to identification of first-arriving direct *P* wave followed by a secondary arriving FZRW.

The procedure discussed so far provides two categories of events and waveforms considered for further analysis: the first with a FZHW followed by a direct *P* phase and the second with a direct *P* arrival followed by a FZRW. The arrival picks of both groups are refined in the process of the particle motion analysis. To summarize the results, we plot for each station the vertical component waveforms of both groups sorted according to the hypocentral distance, aligned on the direct *P* arrival and with the final FZHW and FZRW picks (Table 2, last two columns). This is illustrated in Figure 6 for data recorded by station FP and summarized in Figures 7 and 8 for all used stations. Some stations (e.g., GE north of the Karadere Fault and BV along the Düzce Fault to the east) have no or very few FZHW.

The results plotted in Figures 6 and 7 show a moveout between some FZHW and direct *P* waves with increasing hypocentral distance for events east of stations FI, FP, and to lesser extent for station VO. This indicates the existence of a bimaterial interface across the Karadere Fault at a crustal depth level. In addition, there is a substantial number of FZHW with approximately constant time difference with respect to the direct *P* wave. These "nonmoveout" FZHW are observed at stations FI, MO, WF, FP, and VO. A constant differential

Figure 4. Example of a FZHW and direct *P* wave phases identified based on particle motion analysis. (a) Station (yellow triangle)-event (black circle) geometry in map view. The Karadere and Düzce Faults are colored in red and other fault branches in black. (b) Waveforms recorded from the event shown in Figure 4a separated into the two (top) horizontal and (bottom) vertical components, respectively. The north-south components are plotted with the dashed line. For each waveform the noise is plotted in green. The time window between the onset of the FZHW and the onset of the direct *P* wave is plotted in red. The first portion of the direct *P* wave is plotted in blue. Right after the FZHW arrival the two horizontal components are out of phase, while after the direct *P* arrival the phase shift vanishes. The polarity of the FZHW on the vertical component is positive while the direct *P* wave has a negative first motion in accordance with theory. (c) Three-dimensional particle motion of noise (green), FZHW (red), and direct *P* wave (blue) obtained from the seismograms shown in Figure 4b. The three axes represent the EW, NS, and up-down components of the seismograms. This is a useful tool to compare the changes in particle motion between noise, FZHW, and direct *P* wave in space. (d) Two-dimensional projection of Figure 4c on the EW-NS, EW-vertical, and NS-vertical planes. In the EW-NS plane the FZHW (red) is polarized perpendicular to the fault, while right after the direct *P* arrival (blue) it changes toward the event-station back azimuth as expected. This image is useful for future refining of FZHW and direct *P* wave picks if necessary. In the two other planes one can see the changes in the incidence angle between noise, FZHW and direct *P* wave. (e) Horizontal particle motion with a moving time window (A-F) and the respective waveforms (below) after *Allam et al*. [2014]. Each particle motion plot corresponds to a time window marked with a square on the waveforms. The red arrow shows the direct *P* pick. The dashed red line on each plot represents the event-station back azimuth. Azimuth of the largest eigenvalue and the ratio of eigenvalues are shown in each window, which is a quantitative tool to track the changes of direction and amplitude between noise, FZHW, and direct *P* wave arrivals. The FZHW onset is seen at the end of plot B and at the beginning of plot C. The arrival of the direct *P* wave is seen at plot D.

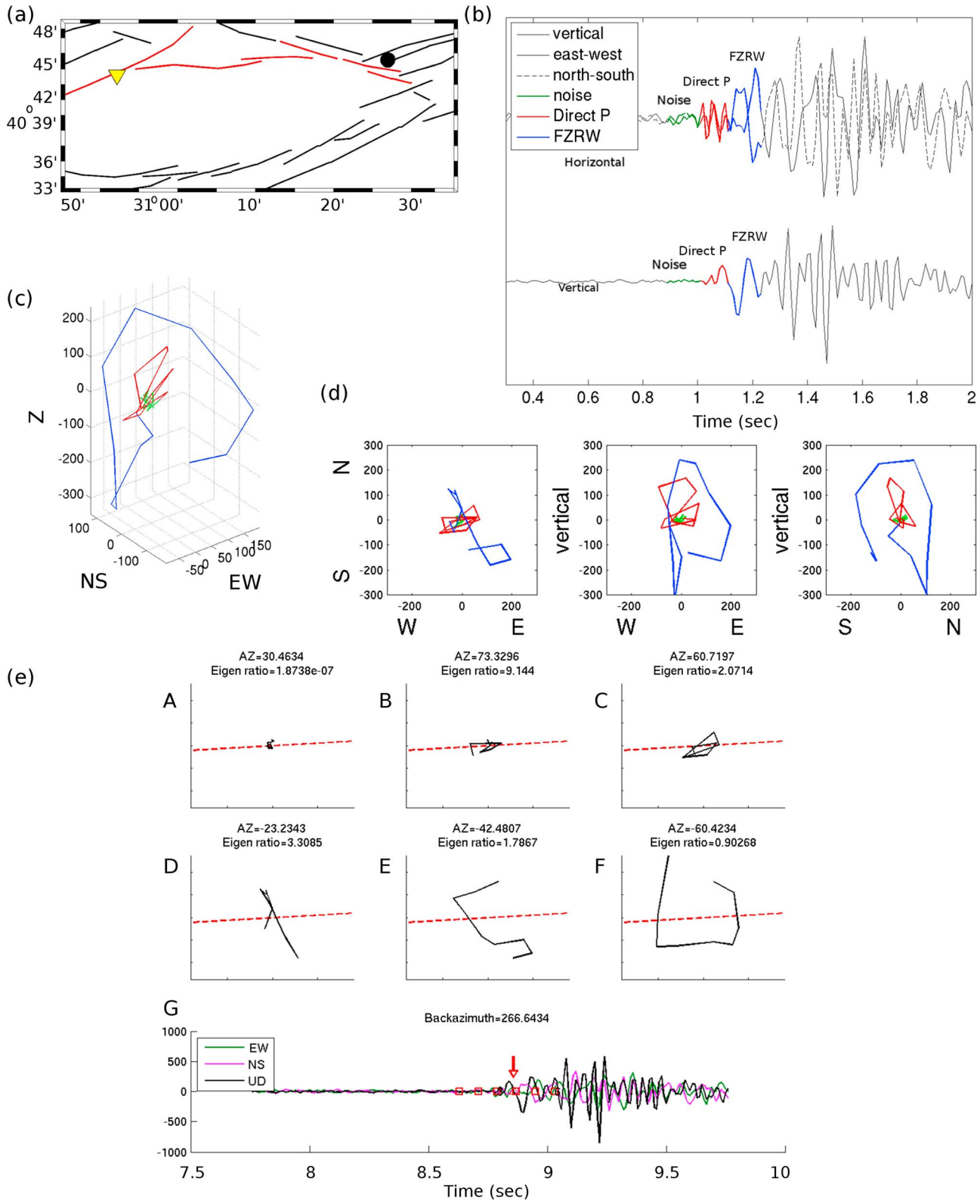

Figure 5. Example of a fault-zone reflected wave (FZRW) and direct *P* phases identified based on polarization analysis. All plots in subfigures are similar to Figure 4. (d) Two-dimensional particle motion plots. In the EW-NS plane, one can see that the direct *P* wave in red is coming from the epicenter and the later reflected phase in blue comes from the fault normal direction. This key difference from Figure 4d distinguishes between the two groups with FZHW or FZRW. The NS-vertical plane shows that the FZRW comes from the north corresponding to the Karadere segment. (e) The red arrow marks the FZRW arrival corresponding to plot D in Figure 5e.

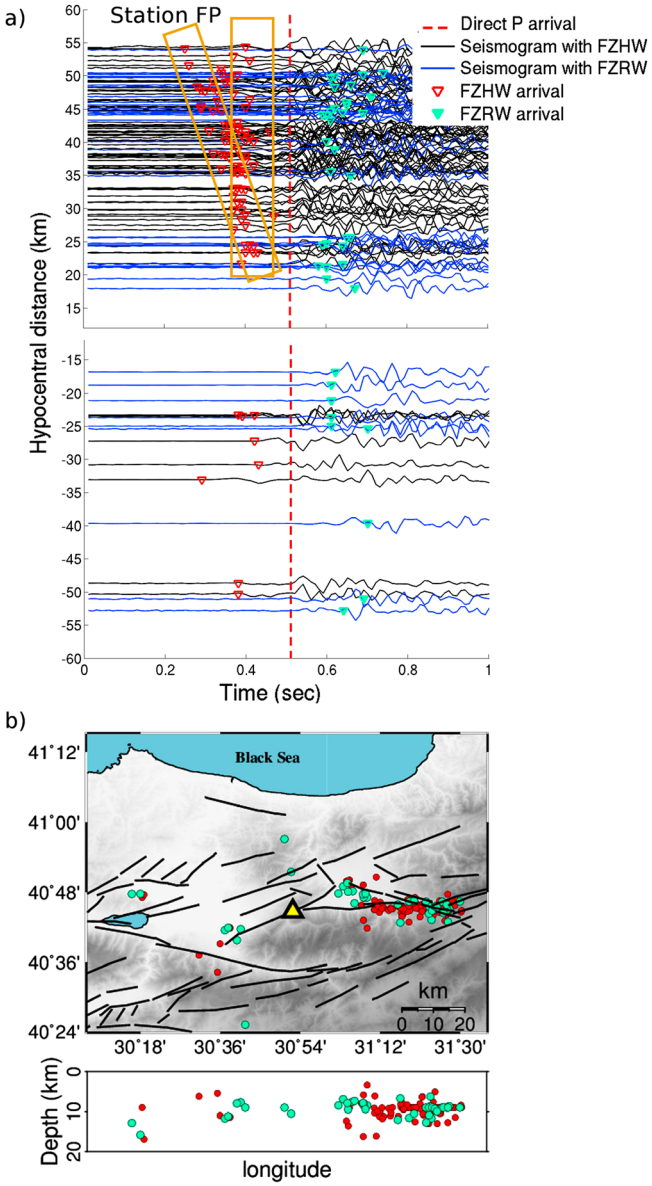

Figure 6. (a) Vertical component waveforms recorded by station FP with refined identification of direct *P* waves, FZHW, and FZRW based on the particle motion analysis illustrated in Figures 4 and 5 and explained in the text. Waveforms either contain FZHW and direct *P* waves (color coded in black) or direct *P* waves and FZRW (color coded in blue). All seismograms are aligned on the direct *P* arrivals (red dashed line) and plotted with hypocentral distance. Positive and negative distances refer to earthquakes east and west of the station, respectively. FZHW arrivals are marked with red triangles (before the dashed line) and FZRW arrivals are marked with cyan triangles (after the dashed line). FZHW are divided into events showing moveout or nonmoveout of the FZHW with respect to direct *P* arrivals as framed by the yellow rectangles. (b) (top) Epicentral and (bottom) depth distribution of the events plotted in Figure 6a. Station FP is marked by the yellow triangle. Events are color coded as in Figure 6a where red and cyan refer to events producing FZHW or FZRW, respectively.

time between FZHW and direct *P* waves cannot be explained by a deep bimaterial interface. However, it can be produced by a shallow local bimaterial interface that affects the wavefield only near (below) the stations. We analyze and discuss this in more detail below.

Figure 8 displays the epicentral and hypocentral distribution of events producing "moveout" and nonmoveout FZHW at the different stations. Figure 9 shows the events producing FZHW at five stations, color coded based on the time difference between the FZHW and direct *P* arrivals. We observe that events producing moveout FZHW (warmer colors in Figure 9) at stations FI and FP are located east of the stations and below 8–10 km depth. Moreover, for station FI one can see a change from blue to red colors for increasing depth and toward the east reflecting the moveout events. For station FP, a group of events with constant high moveout between FZHW and direct *P* waves is observed at a longitude of 31.4° with a depth between 6 and 14 km. These events may sample higher velocity contrast across the fault compared to the remaining seismicity. No systematic pattern between FZHW-*P* differential time and hypocenter location is observed for stations MO and VO located within the Izmit rupture/damage zone [*Ben-Zion et al.*, 2003] and station WF south of the Karadere Fault.

To infer on common characteristics of the moveout and nonmoveout FZHW observed at different stations, we combine all final FZHW picks from stations FI, MO, WF, FP, and VO, plotting them with increasing hypocentral distance aligned with respect to the direct *P* pick (Figure 10a). A scattered but somewhat consistent pattern can be seen with a general average slope for the moveout picks and a uniform differential time for the nonmoveout picks. The substantial scatter potentially reflects the heterogeneity of the structures below the different stations. We note that the summary plot in Figure 10a has overlapping symbols on top of each other. To better visualize the results we show in Figure 10b density plots associated with bins of 0.02 s and 2 km length resulting in a pick density of up to 7 per bin. The shading results support the existence of two

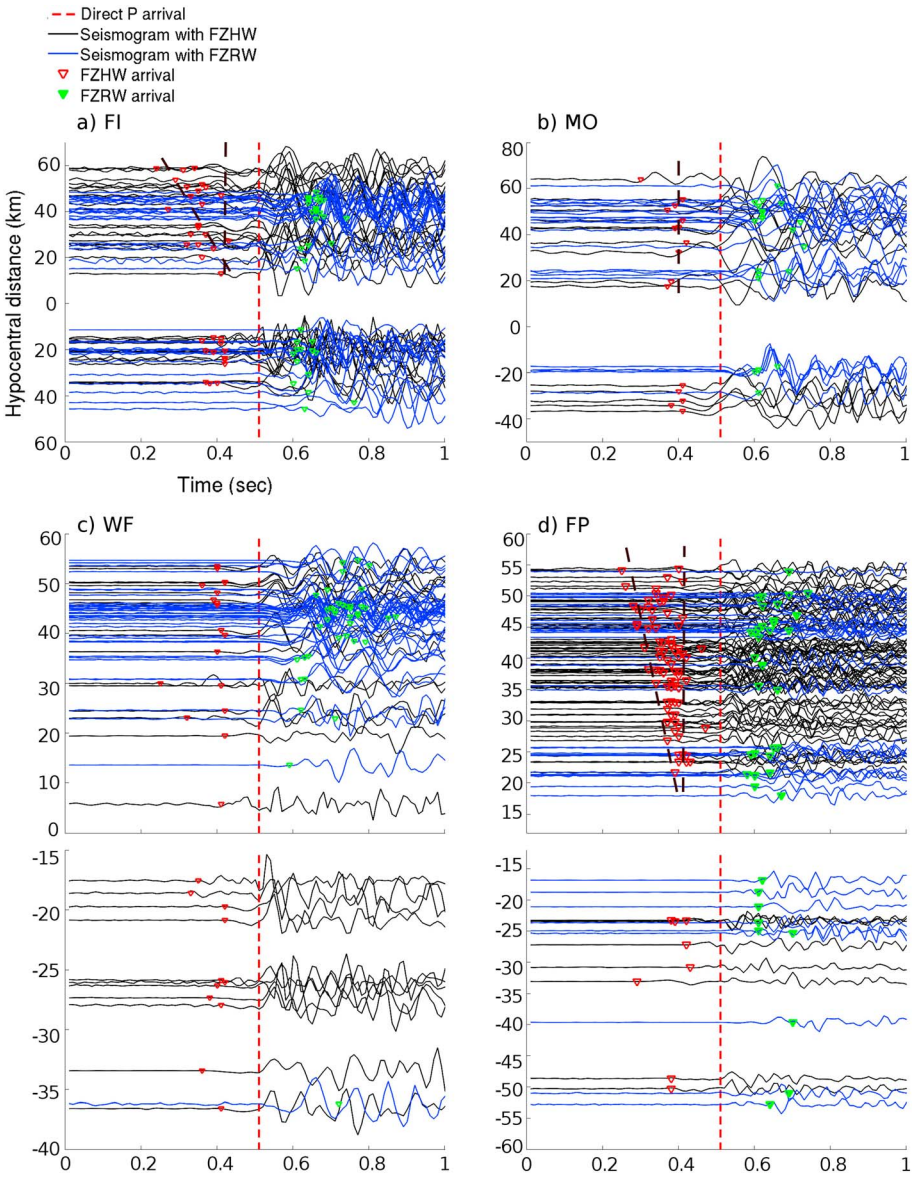

Figure 7. Vertical component seismograms recorded at the seven stations (a) FI, (b) MO, (c) WF, (d) FP, (e) VO, (f) GE, and (g) BV after performing the processing steps shown in Figure 2. A moveout between FZHW and direct *P* waves is seen at stations FI, FP (and to a lesser extent also VO), while mostly a constant offset between FZHW and direct *P* waves can be identified at all stations with FZHW. Station GE located farther away at the northern side of the fault shows almost no FZHW but instead mostly FZRW. Station BV located farther to the east of Düzce Fault also shows no FZHW but instead FZRW. FZRW arrivals (after the dashed lines) are marked with green triangles and the rest of symbols are as in previous figures.

main average patterns with a consistent slope for the moveout FZHW picks and a stable differential time for the nonmoveout picks.

To estimate the average properties of the bimaterial interfaces affecting the wavefields recorded by stations FI, MO, WF, FP, and VO, we use a single pick from each bin in Figure 10b, to reduce the influence of multiple picks with same information, when calculating the change (moveout) of differential times versus propagation distance. This is done in Figure 11a where we separate the remaining FZHW picks into two groups of moveout (blue triangles) and nonmoveout (open red squares) arrivals. Some picks are common to the overall patterns of both groups and are considered in the estimates associated with the two groups. The locations of the events generating the wave arrivals are shown in Figure 11b. A least squares fitting is done for the moveout group separately to either general East or West direction from the stations (positive and negative hypocentral

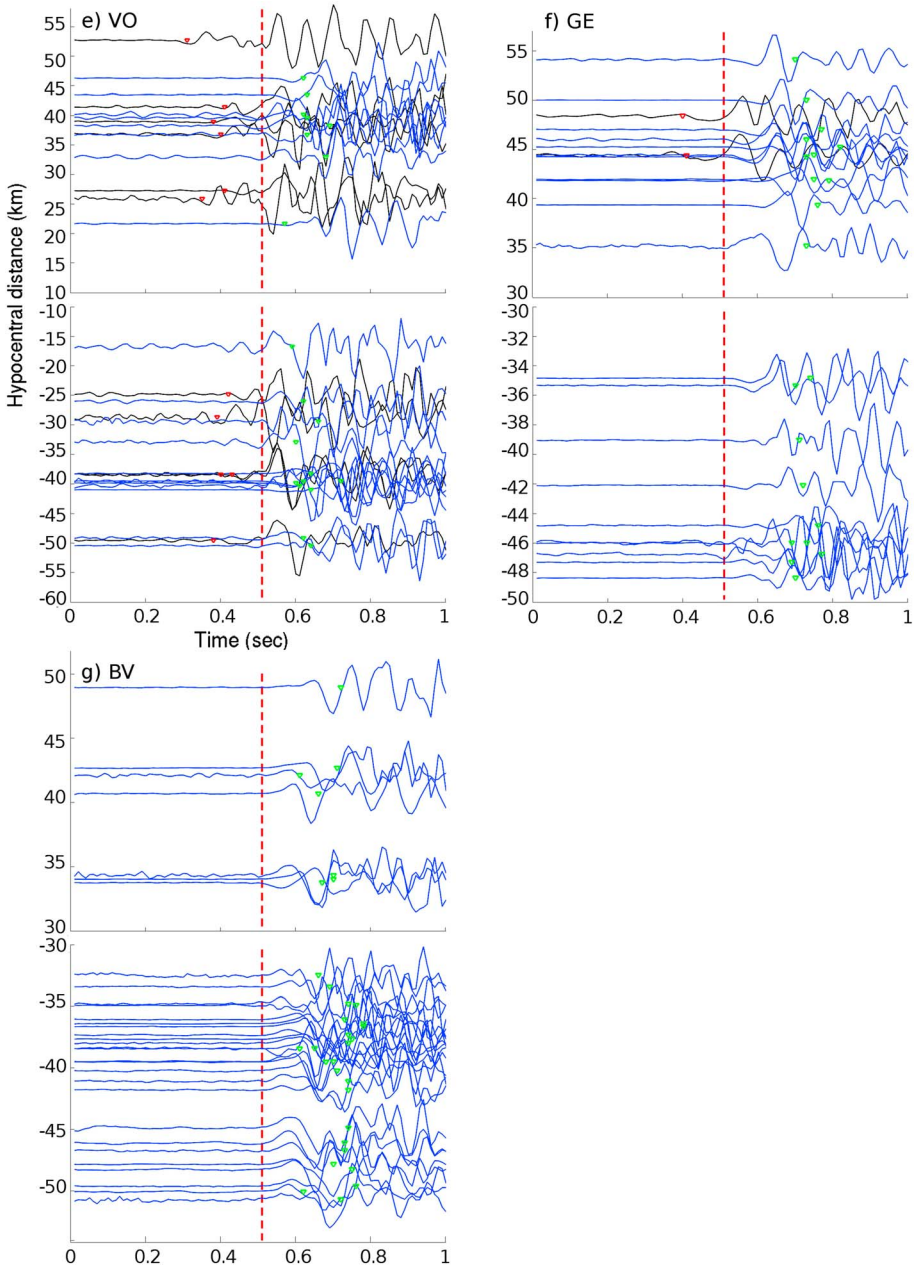

Figure 7. (continued)

distances). The slopes are used in conjunction with equation (2) to estimate the average velocity contrast (AVC) associated with that direction. Assuming in equation (2) that the average *P* wave velocity for the depth section (up to 18 km) producing moveout FZHW is 6 km/s, gives the AVC values (2.87% to 3.91%) indicated in Figure 11a. Using instead an average *P* wave velocity of 5 km/s representative of shallower crustal depth decreases somewhat the AVC values (2.39% and 3.25%).

Two types of errors produce uncertainties in the estimated velocity contrast across the fault. These are the location accuracy of the seismic events and the picking accuracy for the different wave used types (mainly FZHW since they have less accurate arrivals than the direct *P* waves). The average location uncertainty for the hypocenters is about 2–3 km [*Seeber et al.*, 2000; *Ben-Zion et al.*, 2003]. The average picking accuracy for the FZHW based on the automatic picker followed by manual changes based on the particle motion analysis is about 0.02 s. This results in a standard deviation for the slopes at positive and negative hypocentral

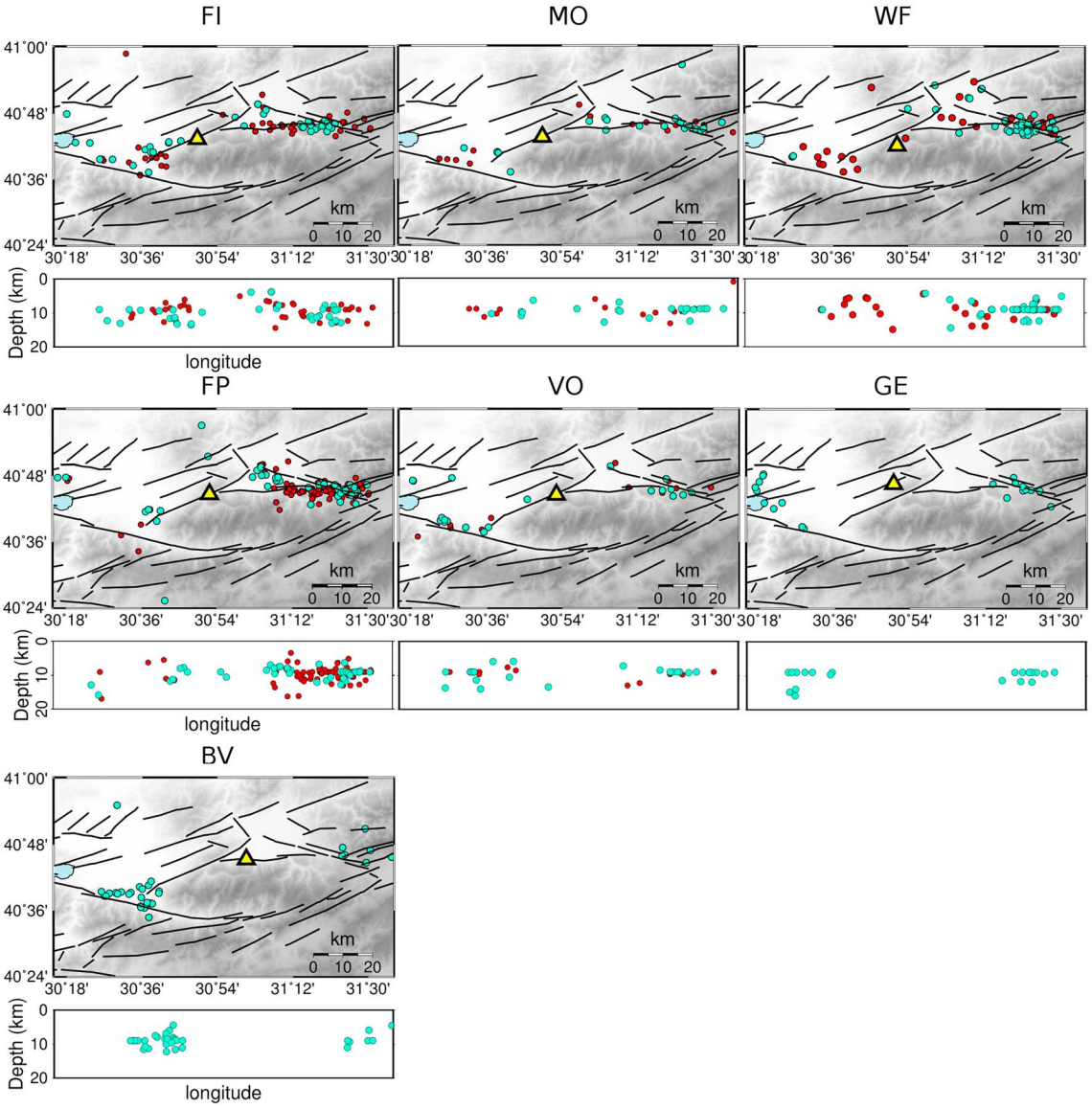

Figure 8. (top) Epicentral and (bottom) depth distribution of events for the seven stations shown in Figures 7a–7g. Symbols are as in Figure 6b.

distances of 0.17 and 0.08, respectively. The slopes were calculated under the assumption that the time difference between FZHW and direct *P* arrivals has to be zero at zero hypocentral distance (required by theory). The resulting uncertainty for the average velocity contrast of 3.4% is 0.2–0.3% (considering average velocity between 5 and 6.8 km/s for the crustal depth sampled here).

For the nonmoveout group we calculate the median differential time in either direction (solid green squares). We assume that the nonmoveout FZHW arrivals are associated with the edge of a low velocity fault damage zone or trapping structure. Using in equation (2) a differential time of 0.11 s, an average *P* wave velocity of 5 km/s representative of the middle to shallow crust, and $\Delta\alpha$ of 50% for the velocity contrast between the damage zone and surrounding rock [e.g., *Ben-Zion et al.*, 2003; *Allam and Ben-Zion*, 2012; *Zigone et al.*, 2015] provides an estimated length scale of the local bimaterial interface of about 5.5 km. Assuming that this length has on average equal along-strike and depth components suggests that the downdip extension of the local bimaterial interface is approximately $5.5/\sqrt{2} = 3.8$ km. This is of the same order as the estimated depth values of the trapping structure and zone producing elevated fault-related anisotropy in the area [*Ben-Zion et al.*, 2003; *Peng and Ben-Zion*, 2004]. We also observe in Figure 11a that a minimum propagation distance of about 15 km (14 and 17 km toward the west and east, respectively) is needed to produce moveout

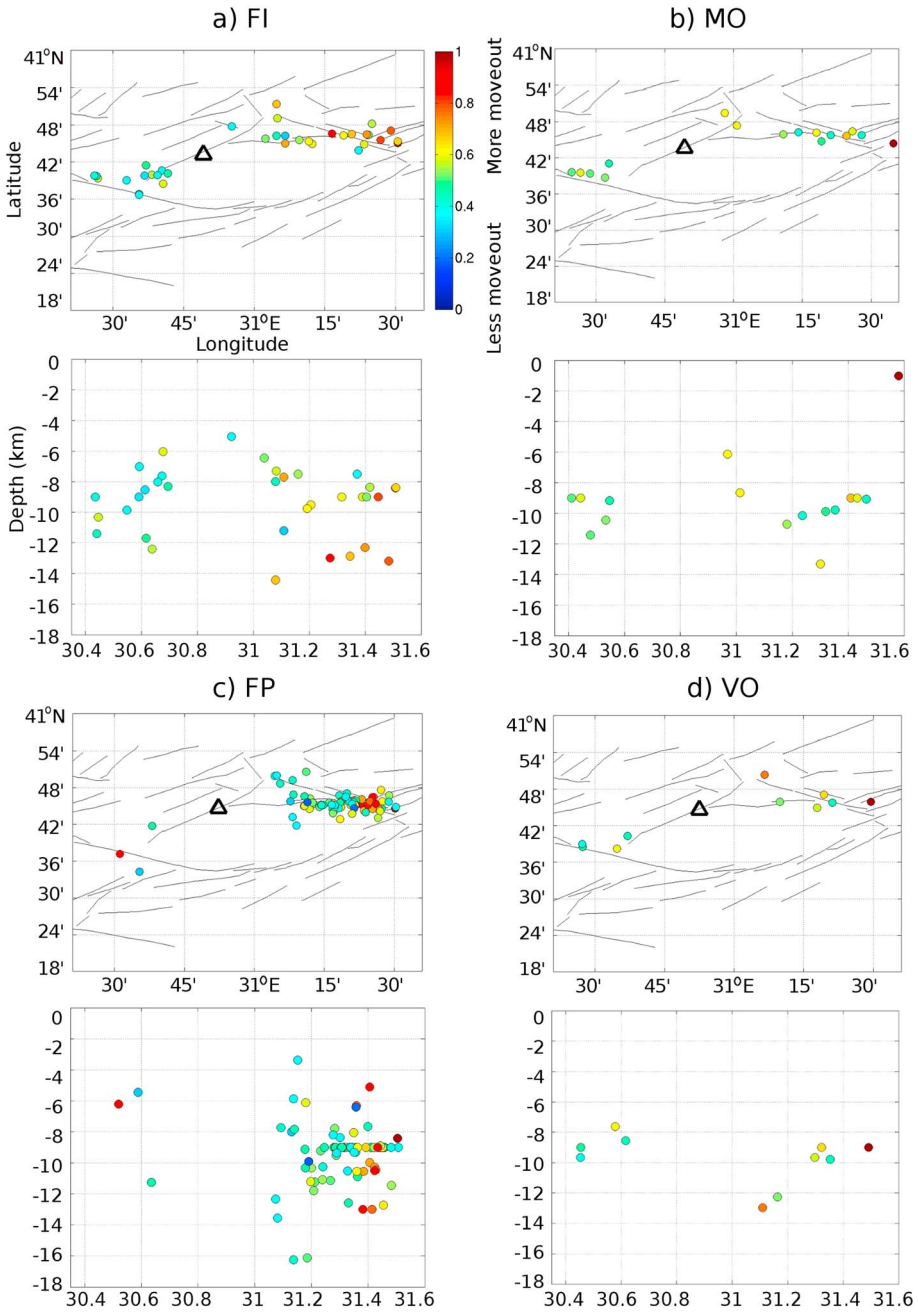

Figure 9. (top) Epicentral and (bottom) depth distribution of events producing FZHW at the five stations (a) FI, (b) MO, (c) FP, (d) VO, and (e) WF, respectively (the other two stations GE and BV did not record enough FZHW, see Figure 7). Events are color coded according to the differential time between direct *P* wave and FZHW. For each station, the differential times are normalized to the respective maximum. For stations FI and FP, a clear increase in differential time with hypocentral distance is observed indicating that the observed moveout is caused by a deep bimaterial interface. For the other stations no first-order moveout between direct *P* waves and FZHW was observed in the seismic sections (see Figure 7).

FZHW in the employed stations. Using in equation (1) a distance of 15 km and $\Delta\alpha$ of 3.4% suggests that the average distance between stations FI, MO, WF, FP, and VO from the deep bimaterial interface is about 4.0 km.

4. Discussion and Conclusions

We analyze about 100,000 waveforms recorded by seven stations located within and around the damage zone of the Karadere Fault at the eastern portion of the 1999 Izmit rupture between the Akyazi and Düzce Basins

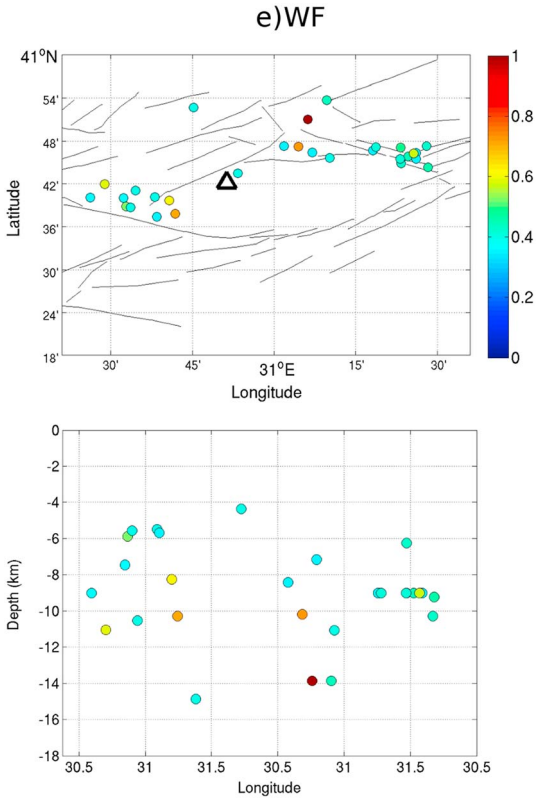

Figure 9. (continued)

(Figure 1). Applying a fully automated recent procedure for identification and picking of fault zone head waves and direct *P* arrivals [*Ross and Ben-Zion*, 2014] results in about 3300 waveforms with two clear separate phases in the early waveforms. These phases are assumed initially to be FZHW followed by direct *P* arrival. Manually revising the automatic picks using particle motion analysis [*Bulut et al.*, 2012; *Allam et al.*, 2014], we find that a substantial subset of these waveforms have first-arriving direct *P* wave (particle motion pointing approximately to the source) followed by a phase that is reflected from a fault interface (particle motion pointing approximately to the fault normal). These secondary phases are labeled Fault Zone Reflected Waves. After the manual analysis and application of strict quality criteria, we are left with 187 high-quality FZHW picks and 215 high-quality FZRW picks.

The tight network configuration with some stations within the fault damage zone allows us to distinguish between two types of FZHW propagating along different bimaterial interfaces in the fault zone structure. The first more commonly observed type of FZHW has a systematic moveout from the direct *P* phases (increasing delay times between the head and direct *P* waves) with increasing propagation distance along the fault. These FZHW are associated with a large-scale bimaterial interface that extends to the bottom of the seismogenic zone and is continuous along strike for tens of kilometers [e.g., *Ben-Zion and Malin*, 1991; *Allam et al.*, 2014]. The second type of FZHW has no moveout from the direct *P* waves (approximately constant delay times) with increasing hypocentral distance and are associated with a shallow local bimaterial interface. Such FZHW have been reported only recently in the context of the Garzê-Yushu Fault in the Tibetan Plateau [*Yang et al.*, 2015] and the San Jacinto Fault zone in Southern California [*Qiu et al.*, 2015].

Observing FZHW from a deep bimaterial fault interface is best done with stations that are ~5 km away from the fault on the slow side, to avoid effects associated with the local damage structure [e.g., *McGuire and Ben-Zion*, 2005]. In the present study, stations MO and VO are located within (or very close to) the trapping structure of the Karadere Fault [*Ben-Zion et al.*, 2003] and are affected primarily by the shallow local bimaterial interfaces of the damage zone. Station WF also records primarily nonmoveout FZHW, suggesting that it is located within a relatively broad damage zone [e.g., *Peng and Ben-Zion*, 2004; *Hamiel and Fialko*, 2007] that extends somewhat to the Almacik block. Stations FP and FI both record ample moveout and nonmoveout FZHW, as well as ample FZRW, suggesting that they are on the slow crustal block near the core damage zone. Stations GE and BV record essentially only FZRW. This suggests that station GE is too far from the deep bimaterial interface (outside x_c of equation (1)), station BV is on the faster velocity block, and that both stations are not close to the edge of a significant broad damage zone that may produce nonmoveout FZHW.

Given the relatively large uncertainties in earthquake locations, we combine all the moveout FZHW and calculate an average velocity contrast across the Karadere Fault at depth. Using equation (2) and assuming an average velocity of 6 km/s, the average velocity contrast east and west of the stations are estimated to be about 2.87% and 3.91%, respectively, in the top 15–18 km. The fact that events down to 18 km depth produce FZHW with large moveout indicates that the deep bimaterial interface extends down to the base of the seismogenic crust. The velocity contrast typically decreases with depth [*Ben-Zion et al.*, 1992; *Lewis et al.*, 2007], so the average velocity contrast in the top 7.5–10 km is expected to be larger than the reported values.

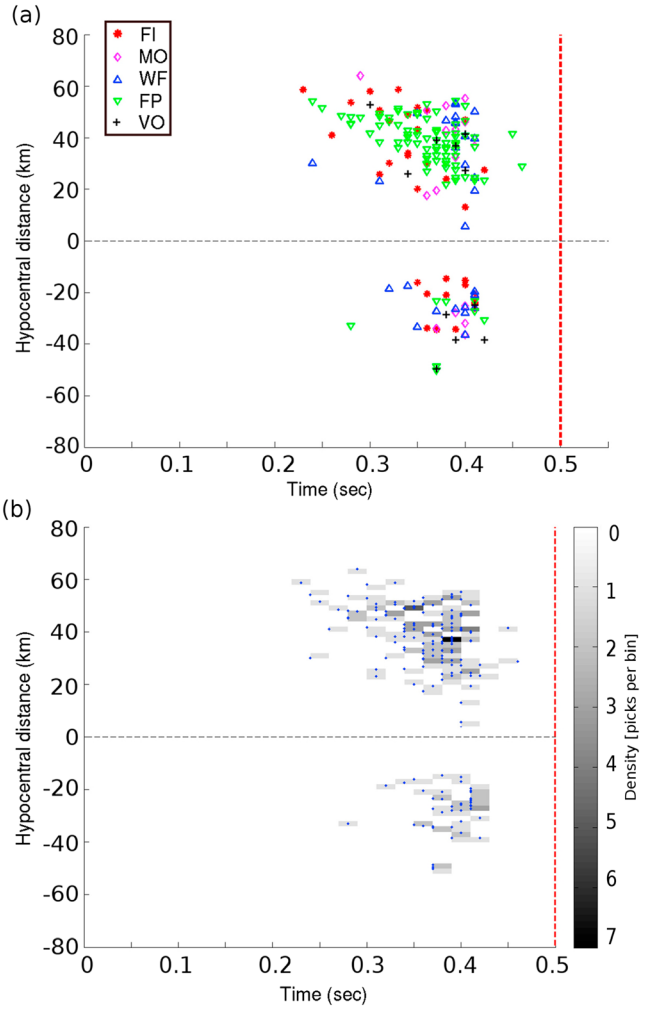

Figure 10. (a) Combined plot of all five stations showing FZHW plotted with respect to the direct *P* arrivals (dashed line) and hypocentral distance. Positive and negative hypocentral distances refer to earthquakes occurring east or west of the respective station. (b) Density plot showing the number of picks within each bin. The density is gray shaded between minimum (zero pick per bin) and maximum (seven picks per bin).

The obtained ~3.4% ± 0.3% average velocity contrast across the fault is somewhat lower than most values observed for other transform faults such as the San Andreas Fault at Parkfield (4–10%) [*Ben-Zion and Malin*, 1991; *Zhao et al.*, 2010] and south of Hollister (10–20%) [*McGuire and Ben-Zion*, 2005; *Lewis et al.*, 2007], the Hayward Fault (3–8%) [*Allam et al.*, 2014], the eastern California shear zone (15%) [*Hough et al.*, 1994], the Garzê-Yushu Fault (5–8%) [*Yang et al.*, 2015], and the Sapanca/Mudurnu segment of the NAFZ (6%) [*Bulut et al.*, 2012].

The lower contrast for the Karadere Fault than the Sapanca/Mudurnu segment [*Bulut et al.*, 2012] may reflect the fact that it is one of two NAFZ branches (Figure 1) and thus presumably has less offset, compared to the single major fault in the Sapanca area farther to the west. The derived relatively low velocity contrast for the Karadere Fault may also be associated in part with the average analysis done jointly for all stations. The relatively low velocity contrast also means that during the particle motion analysis, we could have kept candidate FZHWs with smaller amount of rotation, which would have produced a larger amount of fault zone phases. Our relatively stringent criterion of $>50°$ led to a smaller but presumably higher quality data set. We note that a reduction of the velocity contrast along the NAFZ at the Karadere Fault may have contributed to the arrest of the 1999 Izmit rupture in that area. This is because the dynamic reduction of normal stress along a bimaterial interface increases with increasing velocity contrast up to about 30–40% contrast of *S* wave velocities [e.g., *Ben-Zion and Andrews*, 1998; *Ranjith and Rice*, 2001]. Thus, if the velocity contrast is larger to the west, the Izmit rupture encountered during propagation to the east an increasing frictional strength, due to the diminishing dynamic reduction of normal stress associated with the decreasing velocity contrast. Repeating rupture arrests along the Karadere Fault can contribute to the development of a significant damage zone.

Combining all nonmoveout phases in Figure 10, the mean differential time between the FZHW and direct *P* waves associated with these data is about 0.11 ± 0.02 s. We note that the nonmoveout type of FZHW is observed at stations on both sides of the mapped Karadere Fault, in contrast to the more typical moveout type FZHW that exists only on the slower crustal block. This suggests that the shallow low-velocity body generating the nonmoveout FZHW exists on both sides of the Karadere Fault as shown schematically in Figure 12a. Given the close proximity of the stations to the fault, the low-velocity zone may represent as mentioned highly fractured damaged rocks. Using the average time delay of the nonmoveout phases together with an average *P* wave velocity of 5 km/s for the middle to shallow crust, the depth extent of

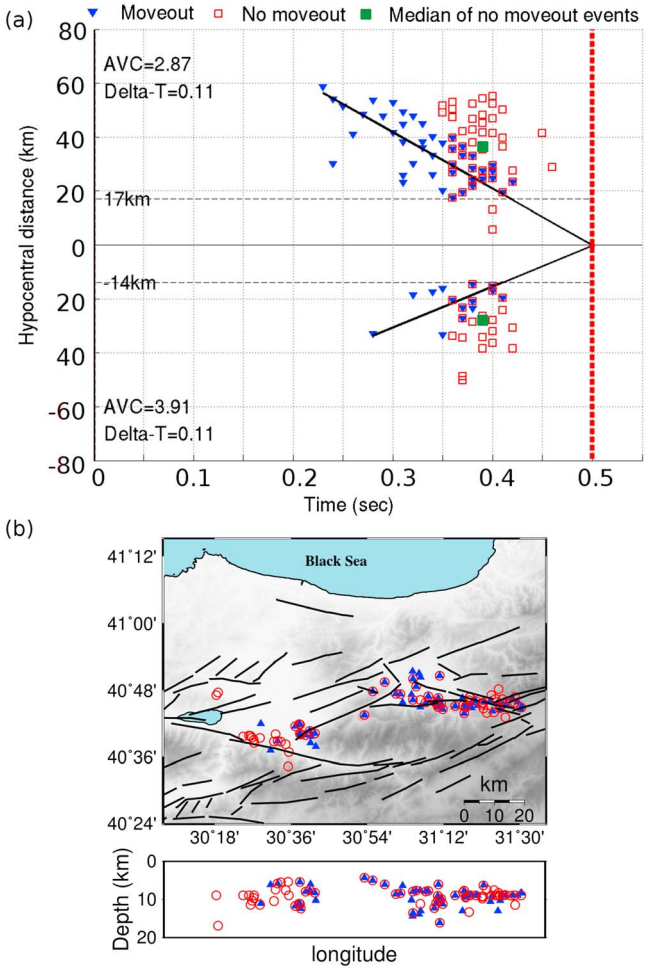

Figure 11. (a) A thinned set of FZHW as in Figure 10a but with picks subdivided into events showing a moveout from the direct *P* wave arrivals (blue filled rectangles) and events reflecting a constant differential time (nonmoveout, red open squares). FZHW picks with both symbols cannot be grouped clearly and thus may belong to moveout- or nonmoveout-producing events. The black lines show the fitted regression lines for the moveout events to the east and west. The green filled squares show the median differential times between FZHW and direct *P* waves for the nonmoveout events. The calculated average velocity contrast (AVC), and differential time between FZHW and direct *P* waves (Delta) for the eastern and western events, respectively, are given in the figure (see text for details). The observed minimum hypocentral distance at which FZHW are observed is 17 km to the east and 14 km to the west. (b) (top) Epicentral and (bottom) depth distribution of the events shown in Figure 11a. The moveout events are shown with filled blue rectangles and nonmoveout events with red circles.

the bimaterial interface at the edge of the low-velocity zone is estimated to be about 3.8 km. Alternatively, using 0.09 s instead of 0.11 s for the mean differential time between the FZHW and direct *P* waves, along with an average *P* wave velocity of 4.7 km/s instead of 5 km/s and 30% velocity contrast between the damage zone and surrounding rock instead of 50%, leads to a depth of 4.7 km. These values are similar to the estimated depth values of the trapping and anisotropic fault structures in the area [*Ben-Zion et al.*, 2003; *Peng and Ben-Zion*, 2004], lending support to the interpretation of this rock body as damaged fault zone layer.

The broader scale shallow low-velocity zone seen by station WF may represent an evolving basin structure related to a progression of the two transtensional features at either end of the Karadere Fault, the Akyazi Basin in the SW, and the Düzce Basin in the NE (Figure 12b). In that case the Karadere Fault, while still being dominated by right-lateral strike-slip deformation as seen during the Izmit earthquake, might be in an early phase of a transition from a local strike slip to an emerging transtensional formation linking the Akyazi and Düzce Basins. This kinematic model is supported by combined strike-slip and normal-faulting mechanisms for Izmit aftershocks [*Bohnhoff et al.*, 2006] in this area. Such progressing basin development is also in accordance with observed positive isotropic source components of Izmit aftershocks [*Stierle et al.*, 2014a, 2014b] and rotations of the local stress tensor orientation [*Ickrath et al.*, 2014, 2015] in the early post-Izmit deformation in the area. However, these observations may also reflect generation of rock damage in the earthquake source volumes [e.g., *Ben-Zion and Ampuero*, 2009; *Ross et al.*, 2015] and a variety of fluid-related effects [e.g., *Hardebeck and Hauksson*, 2001; *Ma et al.*, 2012] rather than the structural evolution suggested above.

In addition to the two types of FZHW, we also identify FZRW that may provide additional information on the internal fault zone structure. However, quantitative interpretation of these waves requires accurate information on hypocenter locations and the fault geometry at depth [e.g., *Li et al.*, 2007; *Yang et al.*, 2014] and is best done with data of a linear array that crosses the fault, so is not attempted here.

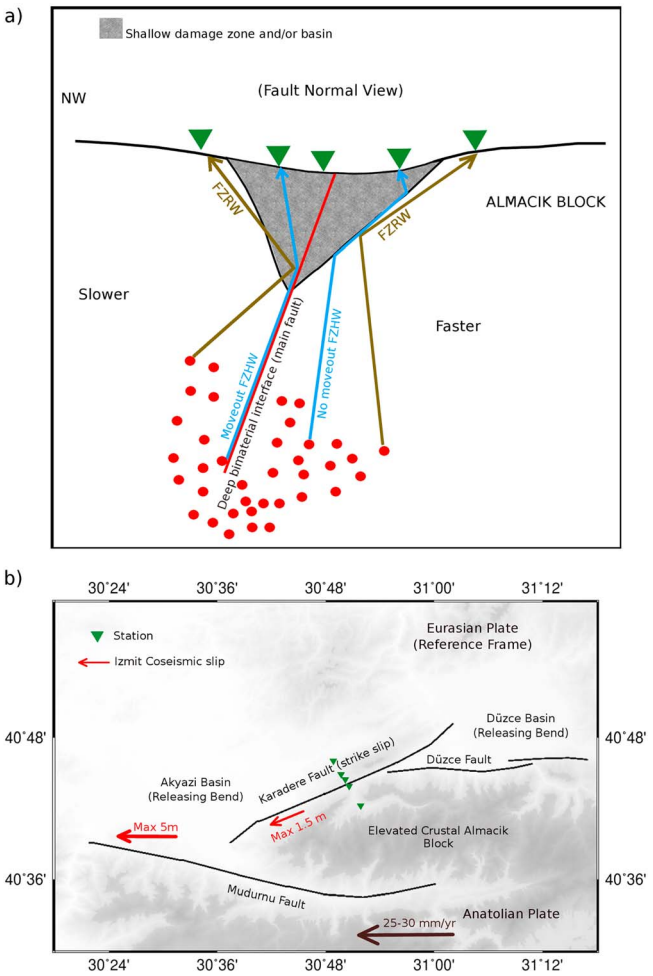

Figure 12. A conceptual model in (a) fault normal and (b) map views. (a) A deep bimaterial interface marked with the oblique red line separates the fast Almacik block at the south (right) from the slower northern side (left). A shallow damage zone or basin is shown in gray. Earthquakes are represented in red circles and two groups of rays, FZRW in dark green and FZHW in blue, reach various stations (green triangles). FZHW propagating along the deep bimaterial interface (main Karadere Fault) produce moveout from the direct *P* waves with increasing hypocentral distance, while FZHW propagating along the shallow interface between the damage zone and the surrounding rocks represent FZHW with no moveout. Additional possible rays of FZRW and nonmoveout FZHW propagating partially or fully through the damage zone are not shown to reduce clutter. (b) Stations are projected on a line across the Karadere Fault to illustrate the various phases plotted in Figures 10 and 11. The red arrows indicate maximum Izmit coseismic slip values and the black arrow indicates the GPS-derived horizontal velocity field with respect to stable Eurasia in the north.

The detailed observations of this work highlight the existence of several types of fault zone interface waves that are recorded by stations close to large fault zones. The classical moveout FZHW generated by a deep bimaterial interfaces exists only on the slower crustal block, but the nonmoveout FZHW and the FZRW can exist generally on both sides of the main fault. These waves can modify considerably the properties of early *P* waveforms recorded near faults from expectations associated with laterally homogeneous structures. The FZHW and FZRW can be utilized to detect and quantify the seismic properties of major fault zone interfaces. As mentioned in the introduction, improved imaging of deep bimaterial and damage zone interfaces can provide important information on various topics of earthquake physics, seismotectonics, and seismic hazard. At minimum, the first-arriving moveout and nonmoveout FZHW should be recognized as such, since their misidentification as direct *P* waves can produce biases in earthquake locations and focal mechanisms [e.g., *Oppenheimer et al.*, 1988; *McGuire and Ben-Zion*, 2005].

Acknowledgments

We acknowledge funding within the Helmholtz Young Investigators Group "From Microseismicity to Large Earthquakes" and from the German Research Foundation within the project Bu2700/1. We thank Fatih Bulut for involvement in an early stage of the work, and Amir Allam and Zach Ross for providing codes for polarization analysis and automatic phase detection. The manuscript benefitted from useful comments by two anonymous referees, an anonymous Associate Editor and Editor Martha Savage. The data used in the paper can be obtained from the Data Management Center (DMC) of Incorporated Research Institutions for Seismology (IRIS): http://ds.iris.edu/SeismiQuery/breq_fast.phtml?net=YJ&yyyymmdd=2000/02/13&hhmmss=161201

References

Allam, A. A., and Y. Ben-Zion (2012), Seismic velocity structures in the southern California plate-boundary environment from double-difference tomography, *Geophys. J. Int.*, *190*(2), 1181–1196, doi:10.1111/j.1365-246X.2012.05544.x.

Allam, A. A., Y. Ben-Zion, and Z. Peng (2014), Seismic imaging of a bimaterial interface along The Hayward Fault, CA, with fault zone head waves and direct *P* arrivals, *Pure Appl. Geophys.*, *171*(11), 2993–3011, doi:10.1007/s00024-014-0784-0.

Ambraseys, N. N. (1970), Some characteristic features of the Anatolian Fault zone, *Tectonophysics*, *9*(2), 143–165.

Ambraseys, N. N., and A. Zatopek (1969), The Mudurnu Valley, West Anatolia, Turkey, earthquake of 22 July 1967, *Bull. Seismol. Soc. Am.*, *59*(2), 521–589.

Ampuero, J.-P., and Y. Ben-Zion (2008), Cracks, pulses and macroscopic asymmetry of dynamic rupture on a bimaterial interface with velocity-weakening friction, *Geophys. J. Int.*, *173*(2), 674–692.

Barka, A. (1992), The north Anatolian Fault zone, paper presented at Annales tectonicae.

Barka, A. (1999), The 17 August 1999 Izmit earthquake, *Science*, *285*(5435), 1858–1859, doi:10.1126/science.285.5435.1858.

Barka, A., H. Akyüz, E. Altunel, G. Sunal, Z. Cakir, A. Dikbas, B. Yerli, R. Armijo, B. Meyer, and J. De Chabalier (2002), The surface rupture and slip distribution of the 17 August 1999 Izmit earthquake (*M* 7.4), North Anatolian fault, *Bull. Seismol. Soc. Am.*, *92*(1), 43–60.

Ben-Zion, Y. (1989), The response of two joined quarter spaces to SH line sources located at the material discontinuity interface, *Geophys. J. Int.*, *98*(2), 213–222.

Ben-Zion, Y. (1990), The response of two half spaces to point dislocations at the material interface, *Geophys. J. Int.*, *101*(3), 507–528.

Ben-Zion, Y. (2001), Dynamic ruptures in recent models of earthquake faults, *J. Mech. Phys. Solids*, *49*(9), 2209–2244.

Ben-Zion, Y., and K. Aki (1990), Seismic radiation from an SH line source in a laterally heterogeneous planar fault zone, *Bull. Seismol. Soc. Am.*, *80*(4), 971–994.

Ben-Zion, Y., and J.-P. Ampuero (2009), Seismic radiation from regions sustaining material damage, *Geophys. J. Int.*, *178*(3), 1351–1356.

Ben-Zion, Y., and D. Andrews (1998), Properties and implications of dynamic rupture along a material interface, *Bull. Seismol. Soc. Am.*, *88*(4), 1085–1094.

Ben-Zion, Y., and P. Malin (1991), San Andreas fault zone head waves near Parkfield, California, *Science*, *251*(5001), 1592–1594.

Ben-Zion, Y., S. Katz, and P. Leary (1992), Joint inversion of fault zone head waves and direct *P* arrivals for crustal structure near major faults, *J. Geophys. Res.*, *97*, 1943–1951, doi:10.1029/91JB02748/.

Ben-Zion, Y., Z. Peng, D. Okaya, L. Seeber, J. G. Armbruster, N. Ozer, A. J. Michael, S. Baris, and M. Aktar (2003), A shallow fault-zone structure illuminated by trapped waves in the Karadere–Duzce branch of the North Anatolian Fault, western Turkey, *Geophys. J. Int.*, *152*(3), 699–717.

Ben-Zion, Y., T. K. Rockwell, Z. Shi, and S. Xu (2012), Reversed-polarity secondary deformation structures near fault stepovers, *J. Appl. Mech.*, *79*(3), 031025.

Bohnhoff, M., H.-P. Harjes, and T. Meier (2005), Deformation and stress regimes in the Hellenic subduction zone from focal mechanisms, *J. Seismol.*, *9*(3), 341–366.

Bohnhoff, M., H. Grosser, and G. Dresen (2006), Strain partitioning and stress rotation at the North Anatolian fault zone from aftershock focal mechanisms of the 1999 Izmit M_w = 7.4 earthquake, *Geophys. J. Int.*, *166*(1), 373–385.

Bohnhoff, M., F. Bulut, G. Dresen, P. E. Malin, T. Eken, and M. Aktar (2013), An earthquake gap south of Istanbul, *Nat. Commun.*, *4*.

Bulut, F., M. Bohnhoff, M. Aktar, and G. Dresen (2007), Characterization of aftershock-fault plane orientations of the 1999 Izmit (Turkey) earthquake using high-resolution aftershock locations, *Geophys. Res. Lett.*, *34*, L20306, doi:10.1029/2007GL031154.

Bulut, F., Y. Ben-Zion, and M. Bohnhoff (2012), Evidence for a bimaterial interface along the Mudurnu segment of the North Anatolian Fault Zone from polarization analysis of *P* waves, *Earth Planet. Sci. Lett.*, *327*, 17–22.

Burchfiel, B., and J. Stewart (1966), "Pull-apart" origin of the central segment of Death Valley, California, *Geol. Soc. Am. Bull.*, *77*(4), 439–442.

Calderoni, G., A. Rovelli, Y. Ben-Zion, and R. Di Giovambattista (2015), Along-strike rupture directivity of earthquakes of the 2009 L'Aquila, central Italy, seismic sequence, *Geophys. J. Int.*, *203*(1), 399–415.

Crowell, J. C. (1974), Origin of late Cenozoic basins in Southern California.

Dor, O., C. Yildirim, T. K. Rockwell, Y. Ben-Zion, O. Emre, M. Sisk, and T. Y. Duman (2008), Geological and geomorphologic asymmetry across the rupture zones of the 1943 and 1944 earthquakes on the North Anatolian Fault: Possible signals for preferred earthquake propagation direction, *Geophys. J. Int.*, *173*(2), 483–504.

Finzi, Y., E. H. Hearn, Y. Ben-Zion, and V. Lyakhovsky (2009), Structural properties and deformation patterns of evolving strike-slip faults: Numerical simulations incorporating damage rheology, *Pure Appl. Geophys.*, *166*(10–11), 1537–1573.

Flerit, F., R. Armijo, G. King, and B. Meyer (2004), The mechanical interaction between the propagating North Anatolian Fault and the back-arc extension in the Aegean, *Earth Planet. Sci. Lett.*, *224*(3), 347–362.

Fukao, Y., S. Hori, and M. Ukawa (1983), A seismological constraint on the depth of basalt–eclogite transition in a subducting oceanic crust.

Görgün, E., M. Bohnhoff, F. Bulut, and G. Dresen (2010), Seismotectonic setting of the Karadere-Düzce branch of the North Anatolian Fault Zone between the 1999 Izmit and Düzce ruptures from analysis of Izmit aftershock focal mechanisms, *Tectonophysics*, *482*(1), 170–181.

Hamiel, Y., and Y. Fialko (2007), Structure and mechanical properties of faults in the North Anatolian Fault system from InSAR observations of coseismic deformation due to the 1999 Izmit (Turkey) earthquake, *J. Geophys. Res.*, *112*, B07412, doi:10.1029/2006JB004777.

Hardebeck, J. L., and E. Hauksson (2001), Crustal stress field in southern California and its implications for fault mechanics, *J. Geophys. Res.*, *106*(B10), 21,859–21,882, doi:10.1029/2001JB000292.

Hartleb, R. D., J. F. Dolan, H. S. Akyüz, T. E. Dawson, A. Z. Tucker, B. Yerli, T. K. Rockwell, E. Toraman, Z. Çakir, and A. Dikbaş (2002), Surface rupture and slip distribution along the Karadere segment of the 17 August 1999 Izmit and the western section of the 12 November 1999 Düzce, Turkey, earthquakes, *Bull. Seismol. Soc. Am.*, *92*(1), 67–78.

Hearn, E. H., R. Bürgmann, and R. E. Reilinger (2002), Dynamics of Izmit earthquake postseismic deformation and loading of the Düzce earthquake hypocenter, *Bull. Seismol. Soc. Am.*, *92*(1), 172–193.

Hough, S., Y. Ben-Zion, and P. Leary (1994), Fault-zone waves observed at the southern Joshua Tree earthquake rupture zone, *Bull. Seismol. Soc. Am.*, *84*(3), 761–767.

Hubert-Ferrari, A., R. Armijo, G. King, B. Meyer, and A. Barka (2002), Morphology, displacement, and slip rates along the North Anatolian Fault, Turkey, *J. Geophys. Res.*, *107*(B10), 2235, doi:10.1029/2001JB000393.

Ickrath, M., M. Bohnhoff, F. Bulut, and G. Dresen (2014), Stress rotation and recovery in conjunction with the 1999 Izmit M_w 7.4 earthquake, *Geophys. J. Int.*, *196*(2), 951–956, doi:10.1093/gji/ggt409.

Ickrath, M., M. Bohnhoff, G. Dresen, P. Martínez-Garzón, F. Bulut, G. Kwiatek, and O. Germer (2015), Detailed analysis of spatiotemporal variations of the stress field orientation along the Izmit-Düzce rupture in NW Turkey from inversion of first-motion polarity data, *Geophys. J. Int.*, *202*(3), 2120–2132.

Jurkevics, A. (1988), Polarization analysis of three-component array data, *Bull. Seismol. Soc. Am.*, *78*(5), 1725–1743.
Kurzon, I., F. Vernon, Y. Ben-Zion, and G. Atkinson (2014), Ground motion prediction equations in the San Jacinto fault zone: Significant effects of rupture directivity and fault zone amplification, *Pure Appl. Geophys.*, *171*(11), 3045–3081.
Le Pichon, X., C. Kreemer, and N. Chamot-Rooke (2005), Asymmetry in elastic properties and the evolution of large continental strike-slip faults, *J. Geophys. Res.*, *110*, B03405, doi:10.1029/2004JB003343.
Lengliné, O., and J. L. Got (2011), Rupture directivity of microearthquake sequences near Parkfield, California, *Geophys. Res. Lett.*, *38*, L08310, doi:10.1029/2011GL047303.
Lewis, M., Y. Ben-Zion, and J. J. McGuire (2007), Imaging the deep structure of the San Andreas Fault south of Hollister with joint analysis of fault zone head and direct *P* arrivals, *Geophys. J. Int.*, *169*(3), 1028–1042.
Li, H., L. Zhu, and H. Yang (2007), High-resolution structures of the Landers fault zone inferred from aftershock waveform data, *Geophys. J. Int.*, *171*(3), 1295–1307.
Lyakhovsky, V., and Y. Ben-Zion (2009), Evolving geometrical and material properties of fault zones in a damage rheology model, *Geochem. Geophys. Geosyst.*, *10*, Q11011, doi:10.1029/2009GC002543.
Ma, K.-F., Y.-Y. Lin, S.-J. Lee, J. Mori, and E. E. Brodsky (2012), Isotropic events observed with a borehole array in the Chelungpu Fault zone, Taiwan, *Science*, *337*(6093), 459–463.
McClusky, S., S. Balassanian, A. Barka, C. Demir, S. Ergintav, I. Georgiev, O. Gurkan, M. Hamburger, K. Hurst, and H. Kahle (2000), Global Positioning System constraints on plate kinematics and dynamics in the eastern Mediterranean and Caucasus, *J. Geophys. Res.*, *105*(B3), 5695–5719, doi:10.1029/1999JB900351.
McGuire, J., and Y. Ben-Zion (2005), High-resolution imaging of the Bear Valley section of the San Andreas Fault at seismogenic depths with fault-zone head waves and relocated seismicity, *Geophys. J. Int.*, *163*(1), 152–164.
Milkereit, C., et al. (2000), Preliminary aftershock analysis of the $M_w = 7.4$ Izmit and $M_w = 7.1$ Düzce earthquake in Western Turkey, in *The 1999 Izmit and Düzce Earthquakes: Preliminary Results*, edited by A. Barka, Ö. Kozaci, and S. Akyüz, pp. 179–187 , Istanbul Technical University, Istanbul.
Oppenheimer, D. H., P. A. Reasenberg, and R. W. Simpson (1988), Fault plane solutions for the 1984 Morgan Hill, California, earthquake sequence: Evidence for the state of stress on the Calaveras Fault, *J. Geophys. Res.*, *93*(B8), 9007–9026, doi:10.1029/JB093iB08p09007.
Ozakin, Y., Y. Ben-Zion, M. Aktar, H. Karabulut, and Z. Peng (2012), Velocity contrast across the 1944 rupture zone of the North Anatolian fault east of Ismetpasa from analysis of teleseismic arrivals, *Geophys. Res. Lett.*, *39*, L08307, doi:10.1029/2012GL051426.
Özalaybey, S., M. Ergin, M. Aktar, C. Tapirdamaz, F. Biçmen, and A. Yörük (2002), The 1999 Izmit earthquake sequence in Turkey: Seismological and tectonic aspects, *Bull. Seismol. Soc. Am.*, *92*(1), 376–386.
Özeren, M. S., and W. E. Holt (2010), The dynamics of the eastern Mediterranean and eastern Turkey, *Geophys. J. Int.*, *183*(3), 1165–1184.
Parsons, T. (2004), Recalculated probability of $M \geq 7$ earthquakes beneath the Sea of Marmara, Turkey, *J. Geophys. Res.*, *109*, B05304, doi:10.1029/2003JB002667.
Peng, Z., and Y. Ben-Zion (2004), Systematic analysis of crustal anisotropy along the Karadere—Düzce branch of the North Anatolian Fault, *Geophys. J. Int.*, *159*(1), 253–274.
Peng, Z., and Y. Ben-Zion (2005), Spatiotemporal variations of crustal anisotropy from similar events in aftershocks of the 1999 *M*7. 4 Izmit and *M*7. 1 Düzce, Turkey, earthquake sequences, *Geophys. J. Int.*, *160*(3), 1027–1043.
Peng, Z., and Y. Ben-Zion (2006), Temporal changes of shallow seismic velocity around the Karadere-Düzce branch of the north Anatolian Fault and strong ground motion, *Pure Appl. Geophys.*, *163*(2–3), 567–600.
Qiu, H., Y. Ben-Zion, Z. Ross, P. Share, and F. Vernon (2015), Internal structure of the San Jacinto Fault zone at Jackass Flat from earthquake data recorded by a dense linear array, paper presented at Abstract of the annual SSA meeting.
Ranjith, K., and J. Rice (2001), Slip dynamics at an interface between dissimilar materials, *J. Mech. Phys. Solids*, *49*(2), 341–361.
Ross, Z. E., and Y. Ben-Zion (2014), Automatic picking of direct *P*, *S* seismic phases and fault zone head waves, *Geophys. J. Int.*, *199*(1), 368–381.
Ross, Z., Y. Ben-Zion, and L. Zhu (2015), Isotropic source terms of San Jacinto fault zone earthquakes based on waveform inversions with a generalized CAP method, *Geophys. J. Int.*, *200*(2), 1269–1280.
Rubin, A. M., and D. Gillard (2000), Aftershock asymmetry/rupture directivity among central San Andreas fault microearthquakes, *J. Geophys. Res.*, *105*(B8), 19,095–19,109, doi:10.1029/2000JB900129.
Schulte-Pelkum, V., and Y. Ben-Zion (2012), Apparent vertical Moho offsets under continental strike-slip faults from lithology contrasts in the seismogenic crust, *Bull. Seismol. Soc. Am.*, *102*(6), 2757–2763.
Seeber, L., J. G. Armbruster, N. Ozer, M. Aktar, S. Baris, D. Okaya, Y. Ben-Zion, and E. Field (2000), The 1999 earthquake sequence along the North Anatolia transform at the juncture between the two main ruptures, *The 1999 Izmit and Duzce Earthquakes: Preliminary Results*, pp. 209–223.
Sengör, A., O. Tüysüz, C. Imren, M. Sakinç, H. Eyidogan, N. Görür, X. Le Pichon, and C. Rangin (2005), The North Anatolian fault: A new look, *Annu. Rev. Earth Planet. Sci.*, *33*, 37–112.
Share, P.-E., Y. Ben-Zion, Z. Ross, H. Qiu, and F. Vernon (2015), Characterization of the San Jacinto Fault Zone northwest of the trifurcation area from dense linear array data, *Abstract of the annual SSA meeting*.
Sibson, R. H. (1986), Rupture interaction with fault jogs, *Earthquake Source Mech.*, *37*, 157–167.
Stierle, E., M. Bohnhoff, and V. Vavryčuk (2014a), Resolution of non-double-couple components in the seismic moment tensor using regional networks—II: Application to aftershocks of the 1999 M_w 7.4 Izmit earthquake, *Geophys. J. Int.*, *196*(3), 1878–1888.
Stierle, E., V. Vavryčuk, J. Šílený, and M. Bohnhoff (2014b), Resolution of non-double-couple components in the seismic moment tensor using regional networks—I: A synthetic case study, *Geophys. J. Int.*, ggt502.
Tibi, R., G. Bock, Y. Xia, M. Baumbach, H. Grosser, C. Milkereit, S. Karakisa, S. Zünbül, R. Kind, and J. Zschau (2001), Rupture processes of the 1999 August 17 Izmit and November 12 Düzce (Turkey) earthquakes, *Geophys. J. Int.*, *144*(2), F1–F7.
Wdowinski, S., B. Smith-Konter, Y. Bock, and D. Sandwell (2007), Diffuse interseismic deformation across the Pacific–North America plate boundary, *Geology*, *35*(4), 311–314.
Wechsler, N., T. K. Rockwell, and Y. Ben-Zion (2009), Application of high resolution DEM data to detect rock damage from geomorphic signals along the central San Jacinto Fault, *Geomorphology*, *113*(1), 82–96.
Wu, C., Z. Peng, and Y. Ben-Zion (2009), Non-linearity and temporal changes of fault zone site response associated with strong ground motion, *Geophys. J. Int.*, *176*(1), 265–278.
Yang, H., Z. Li, Z. Peng, Y. Ben-Zion, and F. Vernon (2014), Low-velocity zones along the San Jacinto Fault, Southern California, from body waves recorded in dense linear arrays, *J. Geophys. Res. Solid Earth*, *119*, 8976–8990, doi:10.1002/2014JB011548.
Yang, W., Z. Peng, and Y. Ben-Zion (2009), Variations of strain-drops of aftershocks of the 1999 İzmit and Düzce earthquakes around the Karadere-Düzce branch of the North Anatolian Fault, *Geophys. J. Int.*, *177*(1), 235–246.
Yang, W., Z. Peng, B. Wang, Z. Li, and S. Yuan (2015), Velocity contrast along the rupture zone of the 2010 M_w6. 9 Yushu, China, earthquake from fault zone head waves, *Earth Planet. Sci. Lett.*, *416*, 91–97.

Zaliapin, I., and Y. Ben-Zion (2011), Asymmetric distribution of aftershocks on large faults in California, *Geophys. J. Int.*, *185*(3), 1288–1304.
Zhao, P., and Z. Peng (2008), Velocity contrast along the Calaveras Fault from analysis of fault zone head waves generated by repeating earthquakes, *Geophys. Res. Lett.*, *35*, L01303, doi:10.1029/2007GL031810.
Zhao, P., Z. Peng, Z. Shi, M. A. Lewis, and Y. Ben-Zion (2010), Variations of the velocity contrast and rupture properties of *M*6 earthquakes along the Parkfield section of the San Andreas Fault, *Geophys. J. Int.*, *180*(2), 765–780.
Zigone, D., Y. Ben-Zion, M. Campillo, and P. Roux (2015), Seismic tomography of the Southern California plate boundary region from noise-based Rayleigh and Love waves, *Pure Appl. Geophys.*, *172*(5), 1007–1032.